RSC Advances

PAPER

View Article Online
View Journal | View Issue

Cite this: *RSC Adv.*, 2026, **16**, 26561

Copper-hollow mesoporous polydopamine-polyacrylic acid nanoplatform enabling photoacoustic imaging-guided photothermal/chemodynamic therapy for osteosarcoma

Haoyu Sun, [a] Zeping Liu,[a] Bowen Chen,[b] Yunkai Bao,[cd] Fenghua Li, [cd] Rui Gu *[a] and Zhenxin Wang [cd]

Osteosarcoma (OS) is an extremely destructive and lethal primary bone cancer, and its treatment remains a great challenge. Herein, a nanoplatform (HMPDA-Cu@PAA) was constructed by loading copper ions into hollow mesoporous polydopamine (HMPDA) and subsequently coating with polyacrylic acid (PAA), which exhibits dual responsiveness to the tumor microenvironment (TME) and exogenous 808 nm near-infrared (NIR) laser irradiation. The mutual conversion of Cu^{+} and Cu^{2+} in the TME endows HMPDA-Cu@PAA NPs with two enzyme-like activities: peroxidase-like (POD-like) and glutathione peroxidase-like (GPx-like) activities. HMPDA-Cu@PAA NPs exhibit a synergistic therapeutic capability that combines chemodynamic therapy (CDT), photothermal therapy (PTT), and the imaging capability of photoacoustic imaging (PAI). The as-prepared HMPDA-Cu@PAA stimulates the generation of toxic hydroxyl radicals (˙OH) in response to the specific TME and depletes intracellular glutathione (GSH) to kill MG63 cells with significant cytotoxic effect. Additionally, the localized temperature increase induced by PTT promotes the generation of toxic ˙OH, thereby achieving synergistic enhancement of PTT/CDT for OS therapy. As a robust nanozyme for PAI-guided multimodal treatment of OS, the HMPDA-Cu@PAA nanoplatform exhibits a remarkable tumor inhibition rate (TIR) of 81.36% in the MG63 tumor-bearing mouse models. Overall, this study presents a versatile and rationally designed nanoplatform, offering a promising paradigm for PAI-guided, TME-activated multimodal OS theranostics.

Received 16th February 2026
Accepted 6th May 2026

DOI: 10.1039/d6ra01369d

rsc.li/rsc-advances

1 Introduction

Osteosarcoma (OS) is a primary malignant bone tumor arising from mesenchymal cell-derived osteogenic precursor cells.[1–3] OS represents the second leading cause of cancer-related mortality among pediatric patients.[4,5] Treatment strategies for OS in clinical settings primarily involve surgical intervention, chemotherapeutic approaches (which encompass both neo-adjuvant and adjuvant therapies), and radiotherapy. Owing to the adverse effects associated with chemoradiotherapy and the inability of surgical intervention to achieve complete tumor eradication, therapeutic outcomes remain unsatisfactory.[6–8] The limitations of current OS treatment methods have compelled us to develop novel, highly effective, and safe treatment approaches, which are crucial for enhancing the overall management level of OS.

Chemodynamic therapy (CDT) represents a treatment approach that leverages Fenton or Fenton-like reactions within the slightly acidic tumor microenvironment (TME) to transform excess hydrogen peroxide (H_2O_2) into highly toxic hydroxyl radicals (˙OH), killing tumor cells.[9] In the TME, H_2O_2 concentrations are often reported at levels of 50–100 μM, whereas normal tissues typically exhibit levels ranging from tens of nM to low μM.[10,11] However, the most commonly used Fenton reaction catalyzed by Fe^{2+} only effectively functions under strongly acidic conditions with pH < 4.[12] Even under the slightly acidic conditions of tumors, its reaction rate and therapeutic efficiency remain relatively low.[13] Under the mildly acidic conditions characteristic of the TME, Cu^{+}-mediated Fenton-like reactions are considerably more efficient than those catalyzed by Fe^{2+}.[14–16] Moreover, the redox cycling between Cu^{2+} and Cu^{+} can be driven by the elevated glutathione (GSH) levels in cancer cells, leading to GSH consumption and thereby enhancing the therapeutic efficacy of chemodynamic therapy (CDT).[16,17] However, CDT monotherapy has often proven insufficient to

[a]Department of Orthopaedic Surgery, China-Japan Union Hospital of Jilin University, Changchun, 130033, PR China. E-mail: gurui@jlu.edu.cn
[b]Department of Thyroid Surgery, General Surgery Center, The First Hospital of Jilin University, Changchun 130021, Jilin, China
[c]Key Laboratory of Electroanalytical Chemistry, Changchun Institute of Applied Chemistry, Chinese Academy of Sciences, Changchun 130022, Jilin, China
[d]University of Science and Technology of China, Hefei 230026, Anhui, China

eradicate tumors, and most copper-based nanoplatforms are now designed as CDT-based combination therapies to achieve more complete tumor clearance.[18,19]

Photothermal therapy (PTT) is a tumor ablation strategy that exploits the photothermal effect for therapeutic purposes. This approach has garnered growing interest in cancer treatment because of its minimally invasive characteristics, significant selectivity, and reduced side effects.[20–22] Dopamine-based materials exhibit great potential in applications such as PTT and photoacoustic imaging (PAI) due to their excellent biocompatibility, biodegradability, and strong near-infrared (NIR) absorption properties, along with their abundant catechol groups that provide anchoring sites for metal ions.[23–26] Compared to single treatment modalities, the synergistic combination of CDT and PTT has been proven to be an effective joint strategy for OS treatment.[24,27,28] Additionally, copper-based materials and polydopamine (PDA) nanomaterials possess outstanding photothermal properties under 808 nm NIR laser irradiation, which not only directly induce tumor cell death through thermal mechanisms but also accelerate Fenton-like reactions in synergistic CDT for tumors.[29,30]

PAI leverages the detection of ultrasonic signals generated by the thermal expansion of tissues after absorbing light energy, featuring characteristics such as non-invasive nature and high sensitivity.[31] Copper-based nanomaterials have garnered significant attention due to their ability to generate photoacoustic signals and synergize various therapies such as PTT and CDT, alongside their high tissue penetration, non-invasive nature, and excellent biocompatibility.[32,33] Moreover, copper-based nanomaterials demonstrate unique advantages such as high yield under mild conditions, controllable structure and size, as well as their favorable safety profile as essential trace elements for human health, particularly in comparison with analogous materials such as gold and silver.[34,35]

In this work, a nanoplatform (HMPDA-Cu@PAA) has been constructed by loading copper ions into hollow mesoporous polydopamine (HMPDA) and subsequently coating with polyacrylic acid (PAA), aiming to enable PAI-guided multimodal treatment (CDT–PTT) of OS. HMPDA-Cu is synthesized through coordination chelation between copper ions and the catechol and amine functional groups of HMPDA. HMPDA-Cu@PAA nanoplatform serves as an efficient photoacoustic contrast agent and PTT agent, while also exhibiting excellent peroxidase-like (POD-like) enzymatic activity. Under 808 nm NIR laser irradiation, the HMPDA-Cu@PAA effectively absorbs light energy and facilitates Cu^{+}/Cu^{2+} redox cycling in the TME to achieve multimodal treatment of OS. The results of *in vivo* experiments demonstrate that HMPDA-Cu@PAA can efficiently suppress OS, highlighting its great potential for solid tumor therapy.

2 Results and discussion

2.1 Construction and characterization of HMPDA-Cu@PAA NPs

The synthesis process and application of HMPDA-Cu@PAA NPs was described in Fig. 1. HMPDA NPs were prepared using a previously reported soft-template method with slight modifications. HMPDA-Cu NPs were synthesized *via* coordination interactions between copper ions and the catechol and amine groups of HMPDA.[36,37] To enhance colloidal stability, HMPDA-Cu NPs were coated with PAA. As shown in Fig. 2a–c, transmission electron microscopy (TEM) confirmed the successful synthesis of HMPDA NPs, sea urchin-like structured HMPDA-Cu NPs, and HMPDA-Cu@PAA NPs, with particle sizes of 149.6 ± 10.8 nm, 170.2 ± 20.5 nm, and 177.8 ± 20.7 nm, respectively. The analysis of TEM element mapping further revealed that the HMPDA-Cu@PAA NPs were consisted of Cu, C, N, and O elements (Fig. 2d). The N_2 adsorption–desorption isotherms of HMPDA and HMPDA-Cu exhibited typical type-IV characteristics, confirming their mesoporous structures. Upon copper coordination, the Brunauer–Emmett–Teller (BET) specific surface area decreased markedly from 120.39 $m^2\ g^{-1}$ to 45.22 $m^2\ g^{-1}$ (Fig. 2e and h). Consistently, the pore size distribution curves revealed a noticeable reduction in the dominant pore diameter of HMPDA-Cu compared with pristine HMPDA (Fig. 2f and h). Zeta potential analysis showed that HMPDA exhibited a negative surface charge, whereas HMPDA-Cu displayed a positive surface charge after the introduction of copper ions. Following the coating with PAA, the Zeta potential of HMPDA-Cu changed from +20.1 ± 0.4 mV to −12.9 ± 0.6 mV (Fig. 2i), further confirming the successful incorporation of Cu ions and the effective encapsulation by PAA. The hydrodynamic diameters of HMPDA, HMPDA-Cu, and HMPDA-Cu@PAA were measured to be 204.4 ± 7.3 nm, 243.3 ± 7.1 nm, and 261.5 ± 5.9 nm, respectively (Fig. 2j). Satisfyingly, the HMPDA-Cu@PAA NPs exhibited considerable stability without evident agglomeration during the 48 h observation (Fig. S1). X-ray photoelectron spectroscopy (XPS) analysis of HMPDA-Cu@PAA NPs revealed five distinct peaks at binding energies of 150.2, 285.4, 400.3, 532.7, and 978.1 eV, corresponding to Cl 2p, C 1s, N 1s, O 1s, and Cu 2p, respectively (Fig. 3a). The C 1s spectrum showed two types of interactions: C–O (288.1 and 286.1 eV) and C–C, (284.8 eV) (Fig. 3b).[38] The N 1s spectrum exhibited three types of interactions: N–H (399.2 eV), N–Cu (399.4 eV), and N=C (400.3 eV) (Fig. 3c).[39,40] The O 1s spectrum displayed peaks at 532.1 and 531.3 eV, corresponding to O–Cu and O–H, respectively (Fig. 3d).[41] The peaks at 198.4 and 200.5 eV in the Cl 2p spectrum originated from the Cl–Cu interaction (Fig. 3e).[42] The Cu 2p spectrum displayed peaks at 932.6 and 954.6 eV corresponding to Cu–Cl, and additional peaks at 956.3 and 933.8 eV matching Cu–O (Fig. 3f), indicating the existence of both monovalent and divalent copper.[43] The above results confirm that copper coordinates with the active groups in HMPDA, such as amino, hydroxyl, and carboxyl groups.[44]

After co-incubating red blood cells with HMPDA-Cu@PAA NPs at concentrations of 100 μg mL^{-1}, 200 μg mL^{-1}, and 500 μg mL^{-1} for 4 h, the hemolysis rates were 1.80%, 2.61% and 4.24%, respectively, all below the safe threshold of 5%. In contrast, the hemolysis of red blood cells in distilled water (ddH_2O) was significantly more pronounced (Fig. S2). These data indicate that HMPDA-Cu@PAA NPs exhibit good biocompatibility in a blood environment, providing a crucial safety basis for their further clinical applications.

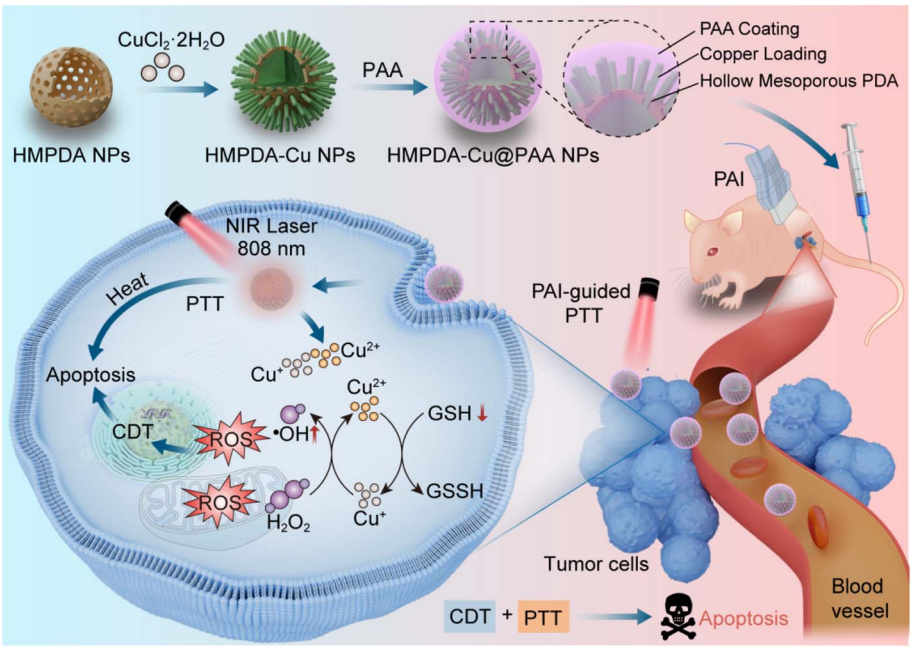

Fig. 1 Schematic illustration of the synthesis process of HMPDA-Cu@PAA and CDT–PTT treatment of osteosarcoma by HMPDA-Cu@PAA NPs.

2.2 Characterization of photothermal properties

To evaluate the photothermal properties of the HMPDA-Cu@PAA NPs, aqueous dispersions at concentrations of 50, 100, and 200 μg mL^{-1} were irradiated with an 808 nm NIR laser at a power density of 2 W cm^{-2} for 10 min. It was noted that with continuous exposure to the 808 nm NIR laser, the temperature increased more significantly as the concentration of HMPDA-Cu@PAA NPs grew (Fig. 4a). At a fixed nanoparticle concentration, increasing the laser power led to a more pronounced temperature elevation of the solution (Fig. 4b). Based on the cooling curve in Fig. S3a and S3b, the photothermal conversion efficiency of the HMPDA-Cu@PAA NPs was measured as 41.44%, which significantly exceeded the photothermal conversion efficiency of HMPDA NPs (23.53%) according to a previous reported formula.[45] The temperature variations of the HMPDA-Cu@PAA NPs remained nearly steady throughout five cycles of heating and cooling (Fig. 4c). Additionally, the TEM micrograph of HMPDA-Cu@PAA NPs showed no significant changes (Fig. S4) after five irradiation cycles, confirming that HMPDA-Cu@PAA NPs had excellent thermal stability. In conclusion, the HMPDA-Cu@PAA NPs exhibit outstanding photothermal efficacy under 808 nm NIR laser irradiation.

2.3 Enzymatic activities evaluation of HMPDA-Cu@PAA NPs

Depleting intratumoral GSH can enhance the efficiency of CDT since the high glutathione levels in tumor cells provide antioxidant defense.[18,46] The HMPDA-Cu@PAA NPs containing divalent copper ions could not only deplete GSH but also be converted into Cu^{+} to promote the Fenton-like reaction. The GSH depletion capability of HMPDA-Cu@PAA NPs was evaluated using the traditional Ellman method (DTNB method) *via* UV-vis spectroscopy and quantitative analysis (Fig. S5). Experimental results demonstrated that as the concentration of HMPDA-Cu@PAA NPs increased, the degree of GSH depletion by HMPDA-Cu@PAA NPs gradually intensified, accompanied by significant color changes in the solution (Fig. 4d). This confirm the outstanding GSH depletion capacity of HMPDA-Cu@PAA NPs, which can effectively reduce GSH levels in tumor cells and enhance CDT treatment efficiency.

The POD-like activity of HMPDA-Cu@PAA NPs was reflected by the degradation of methylene blue (MB), indicating effective ROS generation.[47] The experimental results indicated that as the concentration of HMPDA-Cu@PAA NPs increased (Fig. 4e), pH decreased (Fig. 4f), reaction temperature rose (Fig. 4g), reaction time was prolonged (Fig. 4h), and H_2O_2 concentration increased (Fig. 4i), ROS generation gradually escalated. These results indicate that HMPDA-Cu@PAA NPs can effectively induce ˙OH generation through H_2O_2 decomposition under mildly acidic conditions, demonstrating their excellent Fenton-like catalytic capability in the slightly acidic TME. Under the catalytic action of Cu^{2+}, H_2O_2 can be decomposed to generate ˙OH. Therefore, the ˙OH-generating capability of HMPDA-Cu@PAA NPs was evaluated. In this study, 5,5-dimethyl-1-pyrroline-*N*-oxide (DMPO) was employed as a spin-trapping agent, and ˙OH formation was detected by electron paramagnetic resonance (EPR) spectroscopy. As shown in Fig. S6, the appearance of a 1 : 2 : 2 : 1 peak was observed exclusively in the mixture (pH 6.5) containing HMPDA-Cu@PAA NPs (100 μg mL^{-1}) and H_2O_2 (100 μM), confirming the generation of ˙OH. The POD-like activity of HMPDA-Cu@PAA NPs was evaluated by oxidizing TMB with H_2O_2, as in this catalytic reaction, TMB is oxidized to form oxidized TMB (ox-TMB), a slightly blue product with a characteristic absorption peak at a wavelength of 653 nm (Fig. S7). These results were therefore suggesting that HMPDA-Cu@PAA

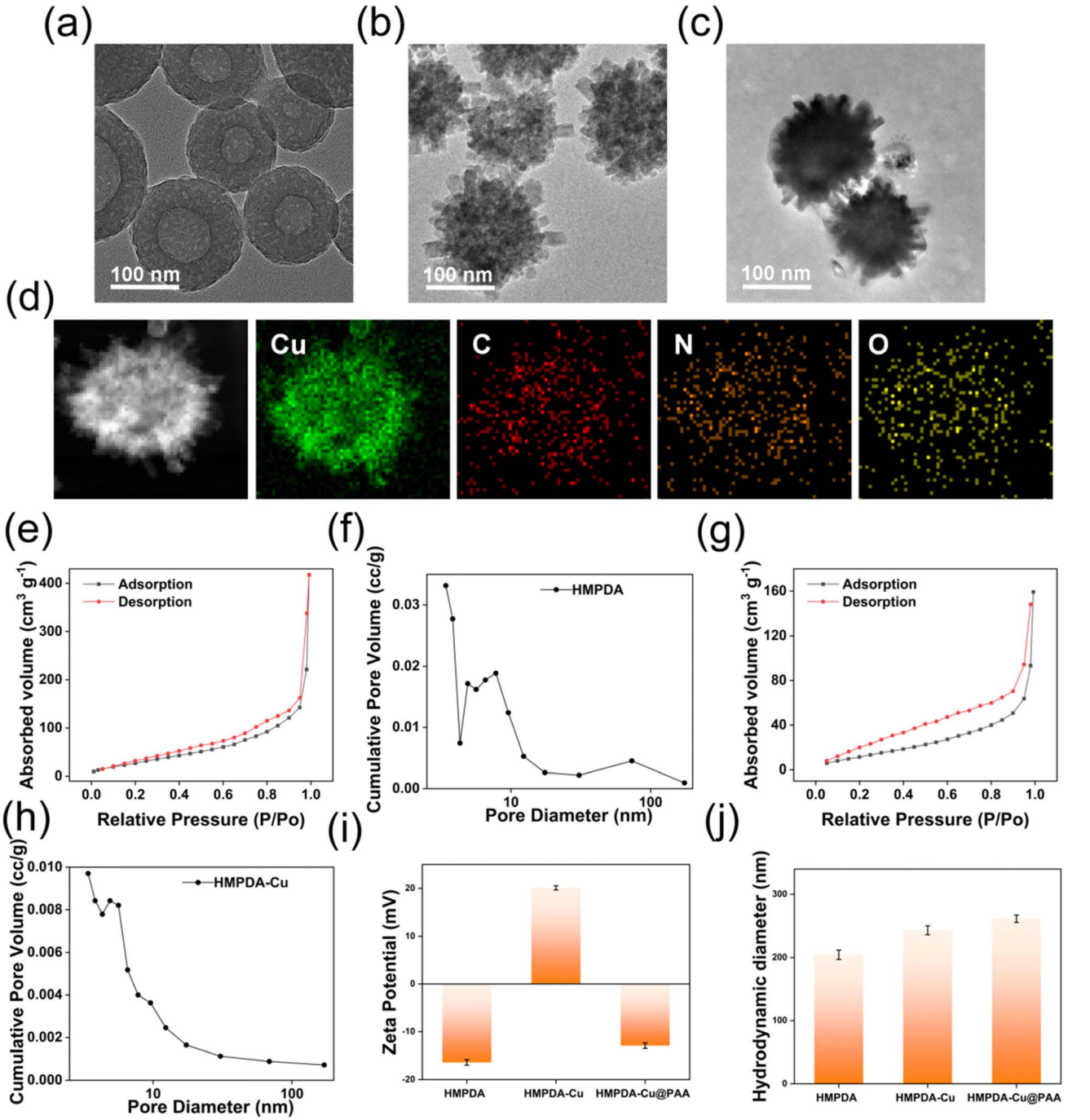

Fig. 2 Characterization of NPs. TEM micrographs of (a) HMPDA, (b) HMPDA-Cu, and (c) HMPDA-Cu@PAA NPs. Scale bar: 100 nm. (d) HAADF-STEM micrograph and EDX elemental mapping of HMPDA-Cu@PAA NPs. (e) N_2 adsorption–desorption isotherm and (f) pore-size distribution of HMPDA NPs. (g) N_2 adsorption–desorption isotherm and (h) pore-size distribution of HMPDA-Cu NPs. (i) Zeta potentials, and (j) hydrodynamic diameters (HDs) of HMPDA, HMPDA-Cu and HMPDA-Cu@PAA NPs.

catalyze the conversion of H_2O_2 to $^{\bullet}OH$ selectively in tumor cells for CDT.

To investigate the catalytic mechanism, XPS was performed to analyze the valence state of Cu in HMPDA-Cu@PAA under different conditions (Fig. S8). The pristine sample is dominated by Cu^{2+} with a Cu^{+} fraction of 33.14%, while GSH treatment markedly increases the Cu^{+} proportion to 59.62%, indicating the reduction of Cu^{2+} to Cu^{+}(Fig. S8a and b). In contrast, H_2O_2 alone induces only a moderate Cu^{+} proportion change (42.39%) (Fig. S8c). Notably, in the presence of both GSH and H_2O_2, the Cu^{+} fraction decreases to an intermediate level (51.65%), suggesting a dynamic interconversion between Cu^{+} and Cu^{2+}(-Fig. S8d). Combined with GSH depletion and ROS generation

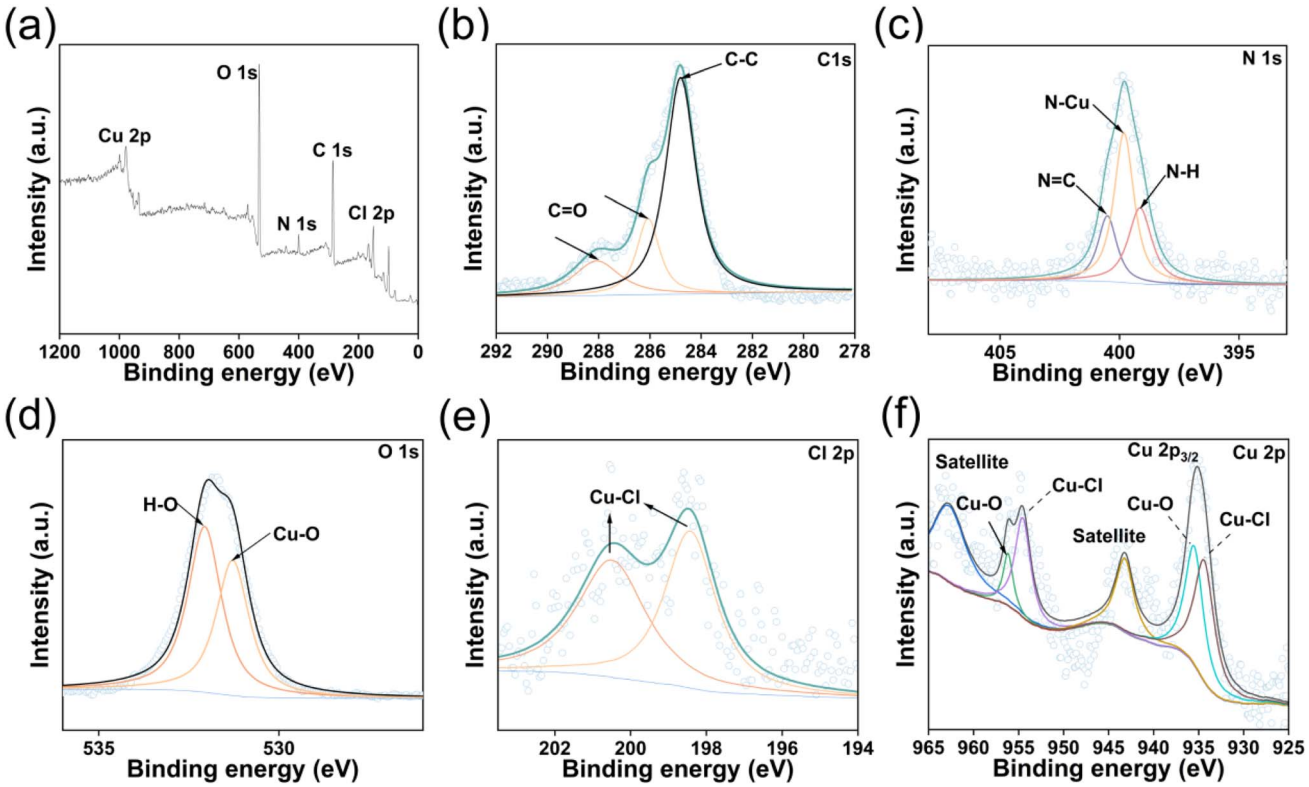

Fig. 3 XPS survey spectra of (a) HMPDA-Cu@PAA NPs, together with the corresponding high-resolution XPS spectra of (b) C 1s, (c) N 1s, (d) O 1s, (e) Cl 2p, and (f) Cu 2p core levels.

results, these findings support a Cu^{2+}/Cu^{+} redox cycling process responsible for the enhanced catalytic activity.

2.4 Combined anti-tumor therapeutic efficacy *in vitro*

To evaluate the *in vitro* antitumor efficacy of the HMPDA-Cu@PAA NPs, their cytotoxicity against MG63 cells was assessed using the MTT assay. The HMPDA-Cu@PAA NPs inhibited the MG63 cell proliferation in a concentration-dependent manner (Fig. 5a). HMPDA-Cu@PAA NPs exhibited low toxicity towards MG63 cells without H_2O_2. Even after 24 h of incubation with 100 μg mL^{-1} HMPDA-Cu@PAA NPs, the viability of MG63 cells still remained at 83.63%. The HMPDA-Cu@PAA NPs plus H_2O_2 (group IV 48.80%), and HMPDA-Cu@PAA NPs plus 808 nm NIR laser (group V 39.81%) groups all exhibited significant inhibition of MG63 cells (Fig. 5b). Notably, the reduction in MG63 cell activity was most pronounced for HMPDA-Cu@PAA NPs plus H_2O_2 and 808 nm NIR laser (group VI 26.89%) group. The observed therapeutic effect can be ascribed to the TME-responsive Fenton-like catalytic behavior of HMPDA-Cu@PAA NPs, coupled with the synergistic action of CDT and PTT. Next, we evaluated the biocompatibility of HMPDA-Cu@PAA NPs with fibroblast L929 cells (Fig. S9). The L929 fibroblast cells exhibited more than 86.65% viability after being incubated with 100 μg mL^{-1} HMPDA-Cu@PAA NPs for 24 h, indicating low cytotoxicity of HMPDA-Cu@PAA NPs.

As shown in Fig. 5c, cell live/death staining tests confirmed the above findings. Both the PTT and CDT groups exhibited stronger tumor cell-killing abilities than PBS group. Notably, the quantity of dead MG63 cells was significantly higher in the combined PTT/CDT group than in the groups involving PTT or CDT alone. This further highlights the synergistic therapeutic benefits of the HMPDA-Cu@PAA NPs.

2.5 Evaluation of ˙OH production capacity

Unlike normal cells, a considerable proportion of cancer cells show heightened levels of ROS, leading to an exacerbated condition of oxidative stress.[43,48] This makes them more susceptible to further damage caused by externally induced ROS from treatments.[49] HMPDA-Cu@PAA NPs exhibited remarkable photothermal properties, which can enhance CDT based on the Fenton-like reaction by increasing temperature, thereby promoting ROS generation to kill cancer cells. To further assess the capability of HMPDA-Cu@PAA NPs to generate ROS in MG63 cells, we employed the green fluorescence probe DCFH-DA. When 808 nm NIR laser or H_2O_2 was used alone, only weak green fluorescence was observed. Bright fluorescence was observed in the HMPDA-Cu@PAA plus H_2O_2 group, attributed to HMPDA-Cu@PAA's POD-like activities (Fig. 5d). After 808 nm NIR laser irradiation (HMPDA-Cu@PAA plus H_2O_2 and NIR, Group VI), the green fluorescence was further significantly enhanced, confirming the excellent photothermal performance of HMPDA-Cu@PAA in boosting the Fenton-like reaction.

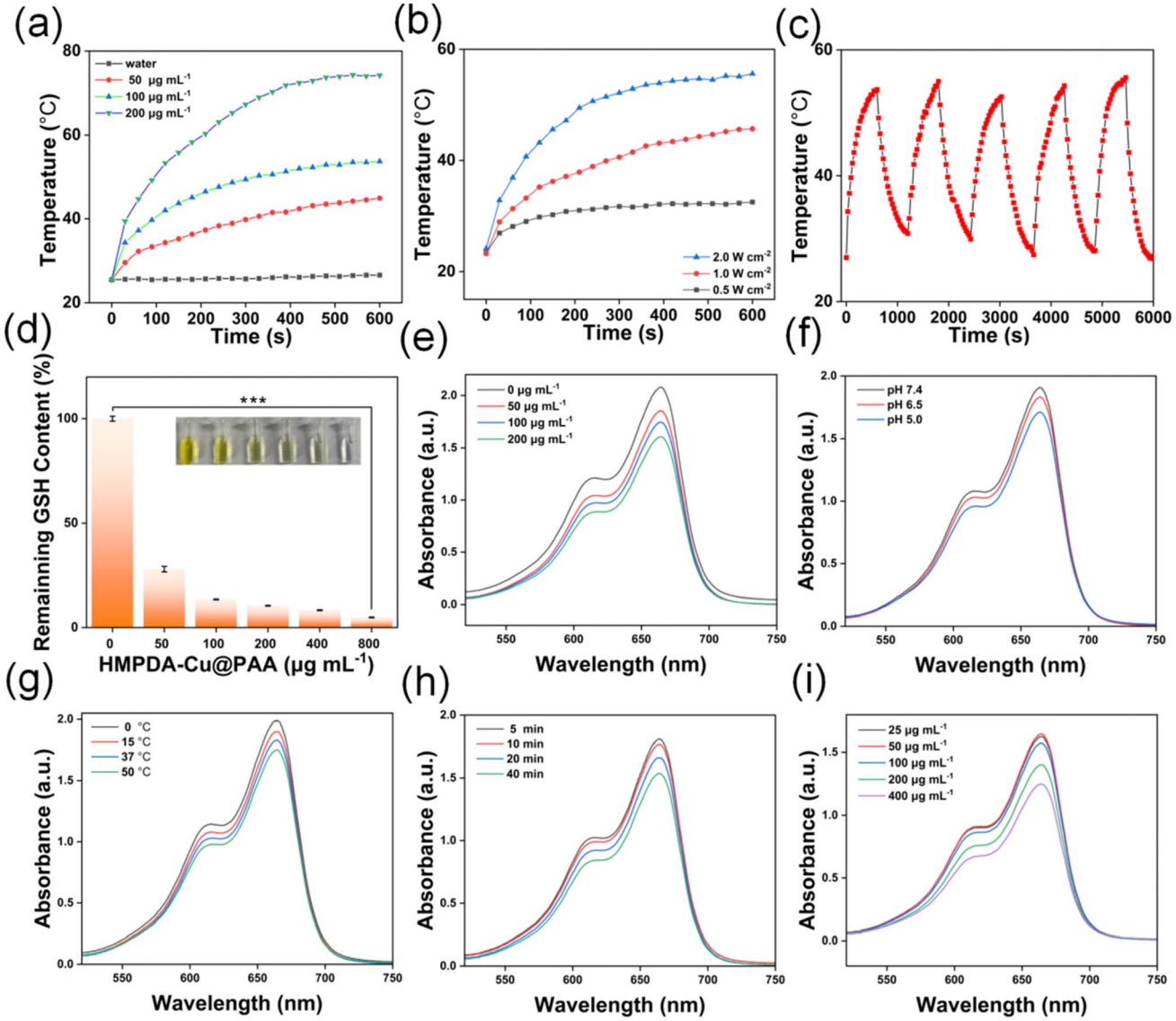

Fig. 4 (a) Temperature elevation curves of HMPDA-Cu@PAA NP dispersions at different concentrations under 808 nm NIR laser irradiation (2.0 W cm^{-2}) for 10 min. (b) Temperature elevation curves of HMPDA-Cu@PAA NP dispersion (100 μg mL^{-1}) under 808 nm NIR laser irradiation at different power densities. (c) Heating and cooling profiles of HMPDA-Cu@PAA NPs irradiated with 808 nm NIR laser during five on/off cycles. (d) Unreacted amounts of GSH after being mixed with 20 μmol L^{-1} GSH and different concentrations of HMPDA-Cu@PAA NPs, and the inset is corresponding photograph. Under different conditions, the UV-vis absorption spectra of MB after undergoing HMPDA-Cu@PAA-mediated redox reactions include the concentration of (e) HMPDA-Cu@PAA NPs, (f) pH, (g) temperature, (h) reaction time, and the concentration of (i) H_2O_2.

2.6 Inhibition of MG63 cell migration and invasion

Given that restraining tumor cell migration and invasion can further augment antitumor therapeutic outcomes, the influence of HMPDA-Cu@PAA NPs on MG63 cell migration and invasion was investigated through wound-healing and transwell invasion assays. As shown in Fig. 5e,the effects of PBS, H_2O_2, HMPDA-Cu@PAA NPs, HMPDA-Cu@PAA plus H_2O_2, HMPDA-Cu@PAA plus 808 nm NIR laser, and HMPDA-Cu@PAA plus H_2O_2 and 808 nm NIR laser treatments on the migration ability of MG63 cells were evaluated using the wound-healing assay. Notably, the healing rate of MG63 cells in the HMPDA-Cu@PAA plus H_2O_2 and 808 nm NIR laser group was significantly lower compared to that of the other groups. This group showed the most efficient inhibitory effect on MG63 cell migration, indicating that the combination of PTT and CDT significantly suppresses MG63 cell migration. Additionally, transwell invasion experiment demonstrated that the HMPDA-Cu@PAA plus H_2O_2 and 808 nm NIR laser group exhibited the lowest number of invasive cells (Fig. 5f), indicating that the combination of PTT and CDT significantly suppresses MG63 cell invasion.

2.7 Evaluation of PAI and photothermal properties

As a highly effective, non-invasive imaging technique, PAI can guide *in vivo* photothermal therapy.[50] Given the significant NIR absorption of HMPDA-Cu@PAA NPs, we evaluated their potential as PAI contrast agents (Fig. S10). After intravenous

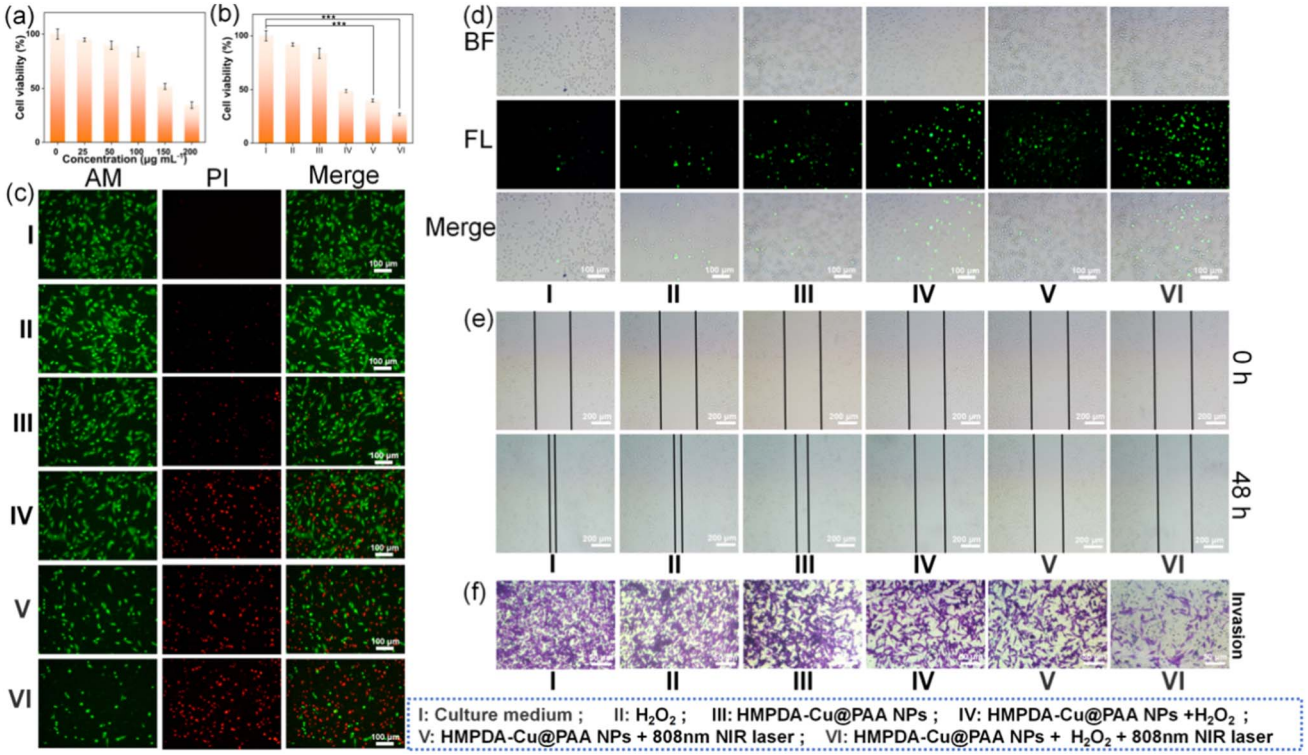

Fig. 5 *In vitro* experiments of HMPDA-Cu@PAA NPs. (a) and (b) cell viability, (c) calicein-AM and PI staining, (d) ROS fluorescence images of MG63 cells co-cultured with HMPDA-Cu@PAA NPs. (e) wound healing width of MG63 cells induced by various formulations measured and photographed at 0 h and 48 h. (f) Representative images of invaded MG63 cells after various formulations. Scale bars: transwell: 50 μm, wound healing: 200 μm. ***$p < 0.001$, **$p < 0.01$, *$p < 0.05$.

injection of HMPDA-Cu@PAA NPs, the appropriate time point for PAI-guided PTT was determined. The tumor exhibited a time-dependent response to the signal, which peaked at 12 h after intravenous administration *in vivo* (Fig. 6a).

To assess the photothermal effect, temperature changes at the tumor location were recorded over 10 min of 808 nm NIR laser exposure, which took place 12 h following the intravenous injection of PBS, and HMPDA-Cu@PAA (Fig. 6b and c). In contrast to the previously mentioned group, the PBS alongside the 808 nm NIR laser group exhibited a minimal temperature rise of 3.7 °C, which indicates that continuous irradiation of the 808 nm NIR laser at a power density of 2.0 W cm^{-2} did not adversely affect the tumor-bearing mice. Conversely, the tumors in the HMPDA-Cu@PAA NPs treatment groups experienced rapid temperature increases of 19.4 °C. These results indicate that the HMPDA-Cu@PAA NPs exhibit significant EPR effects and excellent photothermal conversion efficiency *in vivo*.

2.8 Evaluation of anti-tumor activity

To evaluate the *in vivo* antitumor efficacy of HMPDA-Cu@PAA NPs, a subcutaneous MG63 tumor-bearing mouse model was constructed. After intravenous administration at a tumor size of approximately 4–5 mm, laser irradiation (808 nm, 2.0 W cm^{-2}, 10 min) was applied 12 h post-injection. Tumor volume and body weight were monitored at two-day intervals. At day 14, the mice were sacrificed, and tumors were harvested and weighed for further evaluation (Fig. 7a). The tumor-bearing mice in the HMPDA-Cu@PAA-based treatment groups showed no weight loss, indicating that HMPDA-Cu@PAA NPs led to minimal acute toxicity at the systemic level (Fig. 7b). Tumor volume growth analysis indicated that the HMPDA-Cu@PAA NPs group moderately suppressed tumor growth compared to the control group, whereas the HMPDA-Cu@PAA NPs plus 808 nm NIR laser group exhibited the strongest anti-tumor effect *in vivo* due to the synergistic interaction between CDT and PTT (Fig. 7c). Owing to the synergistic effects of PTT and CDT, HMPDA-Cu@PAA NPs plus 808 nm NIR laser group exhibited the most significant antitumor effect, with a tumor inhibition rate of up to 81.36% (Fig. S11). The results of tumor tissue weight analysis were consistent with the tumor volume growth data, showing that the HMPDA-Cu@PAA NPs plus 808 nm NIR laser group led to a lower mean tumor weight (233.13 mg) than the other groups (Fig. 7d).

The tumor tissues were then obtained for TUNEL staining, along with hematoxylin and eosin (H&E) staining (Fig. 7e). TUNEL and H&E staining indicated that, compared to the control group, the HMPDA-Cu@PAA NPs, and HMPDA-Cu@PAA NPs plus 808 nm NIR laser groups all exhibited larger necrosis areas and higher apoptosis levels. Cells treated with HMPDA-Cu@PAA NPs plus 808 nm NIR laser showed the largest blank areas along with nuclear shrinkage, indicating that the combined therapy of CDT and PTT had significant synergistic antitumor effects.

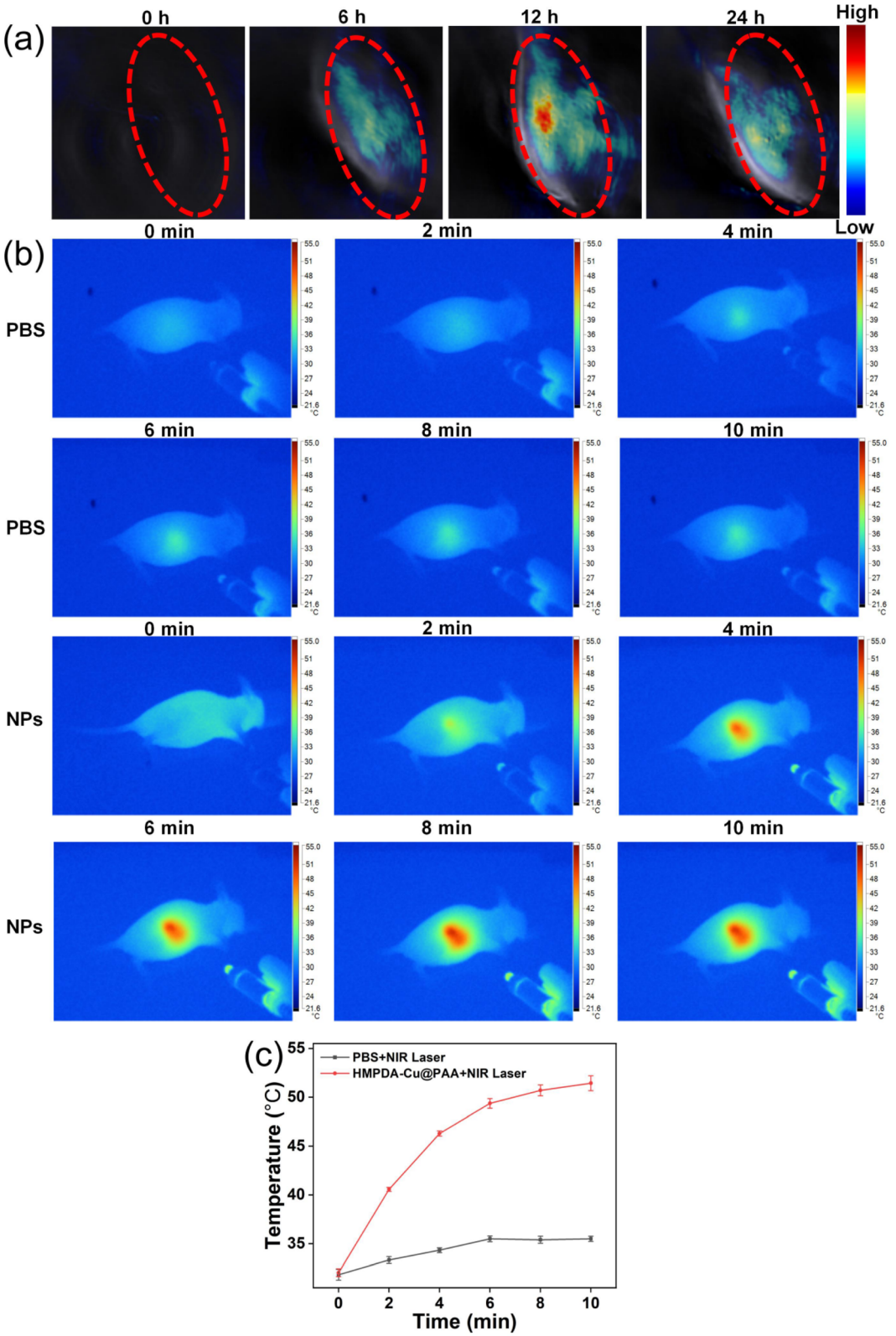

Fig. 6 *In vivo* biological imaging. (a) PAI of tumor captured post-intravenous injection of HMPDA-Cu@PAA NPs (the red circle indicates the tumor). (b) *in vivo* thermal photographs and (c) temperature changes of tumor after intravenous injection of PBS, and HMPDA-Cu@PAA NPs, followed by 808 nm NIR laser irradiation for 600 s.

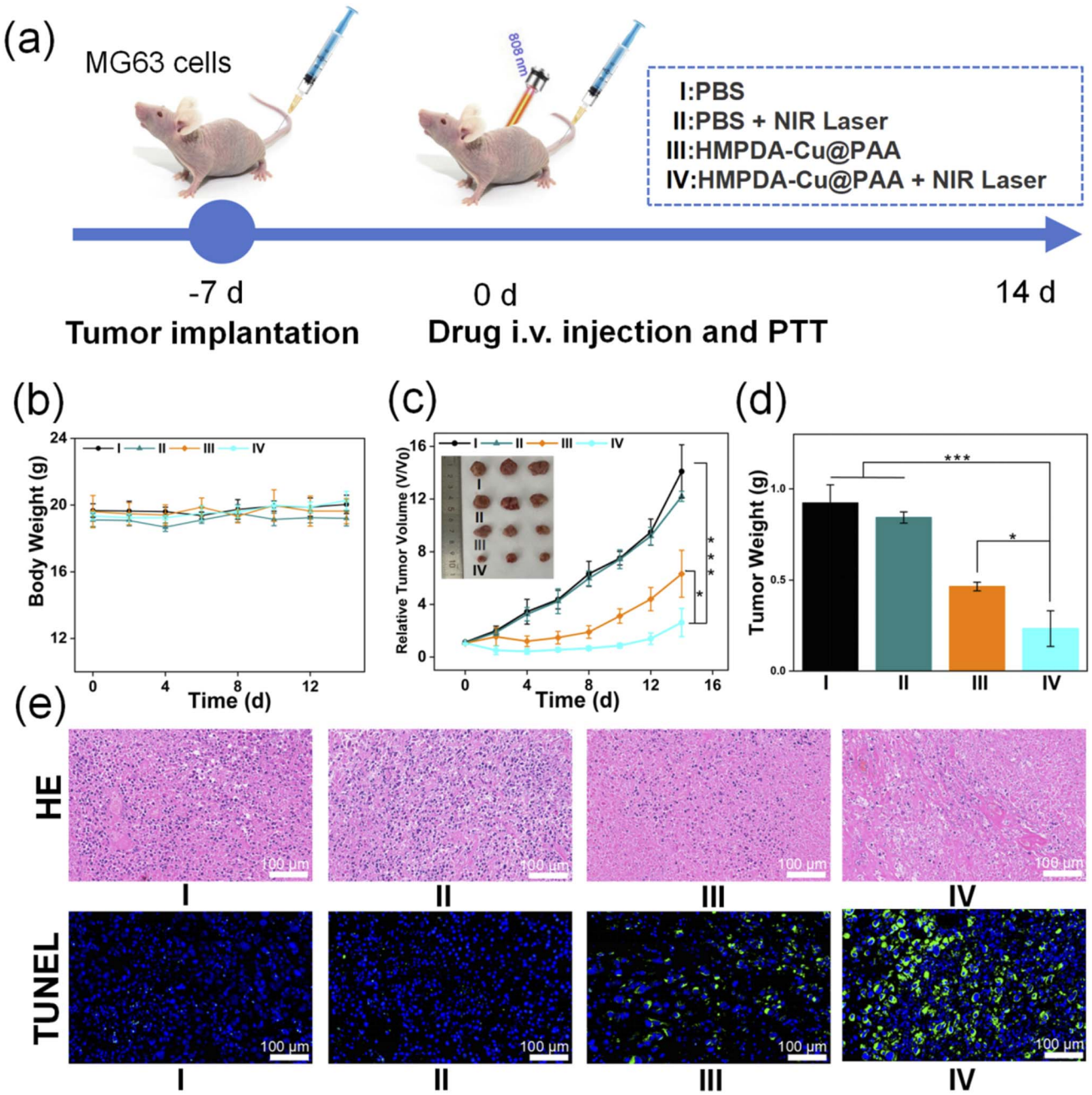

Fig. 7 *In vivo* antitumor assessments. (a) Schematic illustration of the therapeutic process. (b) Curves illustrating body weight change in response to various treatments. (c) Curves showing relative tumor volumes, with the inset presenting typical images of the excised tumors. (d) Tumor weights of MG63 tumor-bearing mice. (e) Representative H&E and TUNEL staining images of tumor tissues after antitumor treatment. Scale bars: H&E: 100 μm; TUNEL: 100 μm. ***$p < 0.001$, **$p < 0.01$, *$p < 0.05$.

2.9 Evaluation of safety of HMPDA-Cu@PAA NPs *in vivo*

Compared with the control group, histological examination of major organs, including the heart, liver, spleen, lungs, and kidneys, revealed no evident pathological abnormalities in the treated groups (Fig. S12). Furthermore, blood samples from MG63 tumor-bearing mice in the PBS and HMPDA-Cu@PAA plus 808 nm NIR laser groups were analyzed to further evaluate hematological parameters and liver function – related indicators. No statistically significant differences were observed in serum biochemical markers or hematological parameters between the two groups (Tables S1 and S2). At 6, 12, and 24 h post-injection, tumor-bearing mice treated with HMPDA-Cu@PAA NPs were euthanized, and major organs and tumors were collected for copper quantification by ICP-MS (Fig. S13). At 6 h, a high Cu level was detected in the liver. The maximum accumulation of copper in the tumor region occurred at 12 h post-injection, approximately 8.56 ± 0.43% ID per g, which is consistent with the PAI results. At subsequent time point,

copper can still be detected in multiple organs, with only minimal residual amounts in organs such as the heart, lungs, and kidneys. These findings suggest that the synthesized HMPDA-Cu@PAA NPs exhibited minimal toxic side effects on MG63 tumor-bearing mice, demonstrating their excellent biological safety *in vivo*.

3 Conclusion

In summary, a multifunctional PAI-guided and therapeutic platform for OS has been developed in this study, enabling synergistic multimodal imaging and combined PTT–CDT treatment. The HMPDA-Cu@PAA nanoplatform exhibits pH-responsive characteristic, PAI capability, enhanced catalytic activity through thermotherapy, glutathione depletion efficacy, and outstanding photothermal performance. HMPDA-Cu@PAA nanoplatform not only enhances the Fenton-like reaction by consuming GSH to generate more toxic $^{\bullet}OH$ but also achieves effective photothermal therapy due to its excellent photothermal properties. This results in a remarkable TIR of 81.36% in a MG63 tumor-bearing mouse model and demonstrates excellent biocompatibility, providing a promising approach for OS treatment.

Author contributions

Haoyu Sun: theoretical calculation, experimental verification, manuscript writing, proofreading. Zeping Liu, Bowen Chen, Yunkai Bao: data management, review and editing. Fenghua Li: investigate, review and editing. Gu Rui, Zhenxin Wang: supervise, review and editing.

Conflicts of interest

The authors declare no competing financial interests.

Data availability

The authors confirm that the data supporting the findings of this study are available within the article. The additional data are available from the corresponding author upon reasonable request.

Supplementary information (SI): additional experimental details, characterization data, supplementary figures and tables, *in vitro* and *in vivo* experimental results and biocompatibility studies. See DOI: https://doi.org/10.1039/d6ra01369d.

Acknowledgements

This study was financially supported by grants from "Medical + X" Cross Innovation Team "Unveiling the List and Taking Command" Construction Project of Bethune Medical College of Jilin University (2024JBGS06) and Jilin Province Science and Technology Development Plan (YDZJ202402063CXJD). The authors acknowledge Dr Wenqi Luo for the assistance provided in the animal experiments.

References

1 Y. Guan, W. Zhang, Y. Mao and S. Li, *Mol. Cancer*, 2024, **23**, 246.
2 W. Liu, L. Li, X. Bai, M. Zhang, W. Lv, Y. Ma, Y. Sun, H. Zhang, Q. Jiang, Q. Yao and Z. Y. Zhang, *Adv. Sci.*, 2025, **12**, e2409870.
3 P. S. Meltzer and L. J. Helman, *N. Engl. J. Med.*, 2021, **385**, 2066–2076.
4 H. C. Beird, S. S. Bielack, A. M. Flanagan, J. Gill, D. Heymann, K. A. Janeway, J. A. Livingston, R. D. Roberts, S. J. Strauss and R. Gorlick, *Nat. Rev. Dis. Primers*, 2022, **8**, 77.
5 V. A. Siclari and L. Qin, *J. Orthop. Surg. Res.*, 2010, **5**, 78.
6 H. Wang, Y. Chen, R. Wei, J. Zhang, J. Zhu, W. Wang, Z. Wang, Z. Wupur, Y. Li and H. Meng, *Adv. Mater.*, 2024, **36**, 2309591.
7 C. V. Sole, F. A. Calvo, E. Alvarez, M. Cambeiro, M. Cuervo, M. San Julian, S. Sole, R. Martinez-Monge and L. Sierrasesumaga, *Radiother. Oncol.*, 2016, **119**, 30–34.
8 L. Aponte-Tinao, M. A. Ayerza, D. L. Muscolo and G. L. Farfalli, *Clin. Orthop. Relat. Res.*, 2015, **473**, 1789–1796.
9 C. Cao, X. Wang, N. Yang, X. Song and X. Dong, *Chem. Sci.*, 2022, **13**, 863–889.
10 S. Chen and Z. Wu, *Oncologie*, 2024, **26**, 899–912.
11 N. Yang, W. Xiao, X. Song, W. Wang and X. Dong, *Nano-Micro Lett.*, 2020, **12**, 15.
12 C. Jia, Y. Guo and F. G. Wu, *Small*, 2022, **18**, e2103868.
13 X. Meng, X. Zhang, M. Liu, B. Cai, N. He and Z. Wang, *Appl. Mater. Today*, 2020, **21**, 100864.
14 Y. Liu, J. D. Wu, Y. H. Jin, W. Y. Zhen, Y. H. Wang, J. H. Liu, L. H. Jin, S. T. Zhang, Y. Zhao, S. Y. Song, Y. Yang and H. J. Zhang, *Adv. Funct. Mater.*, 2019, **29**(50).
15 B. Ma, S. Wang, F. Liu, S. Zhang, J. Duan, Z. Li, Y. Kong, Y. Sang, H. Liu, W. Bu and L. Li, *J. Am. Chem. Soc.*, 2019, **141**, 849–857.
16 Ç. Z. Süngü Akdoğan, E. Akbay Çetin, M. A. Onur, S. Önel and A. Tuncel, *ACS Appl. Mater. Interfaces*, 2025, **17**, 632–649.
17 Y. Ding, Y. Dai, M. Wu and L. Li, *Chem. Eng. J.*, 2021, **426**, 128880.
18 H. Gao, Z. Cao, H. Liu, L. Chen, Y. Bai, Q. Wu, X. Yu, W. Wei and M. Wang, *Theranostics*, 2023, **13**, 1974–2014.
19 L. Xia, M. Chen, C. Dong, F. Liu, H. Huang, W. Feng and Y. Chen, *Adv. Mater.*, 2023, **35**, e2209179.
20 W. Li, J. Yang, L. Luo, M. Jiang, B. Qin, H. Yin, C. Zhu, X. Yuan, J. Zhang, Z. Luo, Y. Du, Q. Li, Y. Lou, Y. Qiu and J. You, *Nat. Commun.*, 2019, **10**, 3349.
21 Y. Liu, P. Bhattarai, Z. Dai and X. Chen, *Chem. Soc. Rev.*, 2019, **48**, 2053–2108.
22 H. B. Park, E. K. An, S. J. Kim, D. Ryu, W. Zhang, C. G. Pack, H. Kim, M. Kwak, W. Im, J. H. Ryu, P. C. W. Lee and J. O. Jin, *ACS Nano*, 2024, **18**, 33366–33380.
23 W. Cheng, J. Nie, L. Xu, C. Liang, Y. Peng, G. Liu, T. Wang, L. Mei, L. Huang and X. Zeng, *ACS Appl. Mater. Interfaces*, 2017, **9**, 18462–18473.
24 Z. Hu, H. Tan, Y. Ye, W. Xu, J. Gao, L. Liu, L. Zhang, J. Jiang, H. Tian, F. Peng and Y. Tu, *Adv. Mater.*, 2024, **36**, e2412227.

25 Y. Tian, M. R. Younis, Y. Tang, X. Liao, G. He, S. Wang, Z. Teng, P. Huang, L. Zhang and G. Lu, *J. Nanobiotechnol.*, 2021, **19**, 365.
26 M. Yang, N. Zhang, T. Zhang, X. Yin and J. Shen, *Drug Deliv.*, 2020, **27**, 367–377.
27 Y. Liang, C. Liao, X. Guo, G. Li, X. Yang, J. Yu, J. Zhong, Y. Xie, L. Zheng and J. Zhao, *Small*, 2023, **19**, e2205511.
28 Y. Xu, L. Yang, M. Li, H. Shu, N. Jia, Y. Gao, R. Shi, X. Yang, Z. Zhang and L. Zhang, *Acta Pharm. Sin. B*, 2024, **14**, 1329–1344.
29 Z. Yan, M. Sun, M. Wang, C. Yin, Z. J. Wei, Z. Zhang, Y. Wang, W. Wang and Z. Yuan, *J. Contr. Release*, 2023, **364**, 371–382.
30 W. X. Zhang, Y. N. Hao, Y. R. Gao, Y. Shu and J. H. Wang, *ACS Appl. Mater. Interfaces*, 2021, **13**, 38127–38137.
31 Q. Fu, R. Zhu, J. Song, H. Yang and X. Chen, *Adv. Mater.*, 2019, **31**, 1805875.
32 X. Zhong, X. Dai, Y. Wang, H. Wang, H. Qian and X. Wang, *Wiley Interdiscip. Rev. Nanomed. Nanobiotechnol.*, 2022, **14**, e1797.
33 W. Zuo, Z. Fan, L. Chen, J. Liu, Z. Wan, Z. Xiao, W. Chen, L. Wu, D. Chen and X. Zhu, *Acta Biomater.*, 2022, **147**, 258–269.
34 S. Yang, Y. Song, Y. Hu, H. Chen, D. Yang and X. Song, *Adv. Healthcare Mater.*, 2023, **12**, 2300410.
35 M. Zhou, M. Tian and C. Li, *Bioconjug. Chem.*, 2016, **27**, 1188–1199.
36 K. Lin, Y. Gan, P. Zhu, S. Li, C. Lin, S. Yu, S. Zhao, J. Shi, R. Li and J. Yuan, *Nanotechnology*, 2021, **32**, 285602.
37 J. Yan, J. Zhang, Y. Wang, H. Liu, X. Sun, A. Li, P. Cui, L. Yu, X. Yan and Z. He, *Adv. Sci.*, 2023, **10**, e2207448.
38 M. Fatkullin, D. Cheshev, A. Averkiev, A. Gorbunova, G. Murastov, J. Liu, P. Postnikov, C. Cheng, R. D. Rodriguez and E. Sheremet, *Nat. Commun.*, 2024, **15**, 9711.
39 W. J. Gammon, O. Kraft, A. C. Reilly and B. C. Holloway, *Carbon*, 2003, **41**, 1917–1923.
40 C. P. Nawarathne, D. G. Aranda, A. Hoque, G. R. Dangel, J. M. Seminario and N. T. Alvarez, *Nanoscale Adv.*, 2024, **6**, 428–442.
41 I. Platzman, R. Brener, H. Haick and R. Tannenbaum, *J. Phys. Chem. C*, 2008, **112**, 1101–1108.
42 Y.-H. Lee, Y.-W. Kim, J.-M. Lim, U.-S. Kang and J.-G. Kim, *npj Mater. Degrad.*, 2026, **10**, 10.
43 X. Li, X. Zhang, L. Song, Y. Li, A. Liu, L. Li, M. D. Nešić, D. Li, L. Peng, C. Wang and Q. Lin, *ACS Nano*, 2024, **18**, 34656–34670.
44 Y. K. Mei, Y. W. Zhu, Y. W. Wei, S. D. Li, X. Zhou, Y. N. Yao and J. Qiu, *RSC Adv.*, 2025, **15**, 13603–13617.
45 Y. Liu, K. Ai, J. Liu, M. Deng, Y. He and L. Lu, *Adv. Mater.*, 2013, **25**, 1353–1359.
46 L.-S. Lin, J. Song, L. Song, K. Ke, Y. Liu, Z. Zhou, Z. Shen, J. Li, Z. Yang, W. Tang, G. Niu, H.-H. Yang and X. Chen, *Angew. Chem., Int. Ed.*, 2018, **57**, 4902–4906.
47 X. Li, Z. Meng, L. Guan, A. Liu, L. Li, M. D. Nešić, B. Yang, W. Qu and Q. Lin, *Chem. Eng. J.*, 2024, **487**, 150545.
48 S. Guo, W. Xiong, J. Zhu, J. Feng, R. Zhou, Q. Fan, Q. Zhang, Z. Li, J. Yang, H. Zhou, P. Yi, Y. Feng, S. Yang, X. Qiu, Y. Xu and Z. Shen, *Biomaterials*, 2023, **302**, 122300.
49 J. Noh, B. Kwon, E. Han, M. Park, W. Yang, W. Cho, W. Yoo, G. Khang and D. Lee, *Nat. Commun.*, 2015, **6**, 6907.
50 W. Ni, J. Wu, H. Fang, Y. Feng, Y. Hu, L. Lin, J. Chen, F. Chen and H. Tian, *Nano Lett.*, 2021, **21**, 7796–7805.